Northumbria Research Link

ORIGINAL ARTICLE

The effects of receiver arrangement on velocity analysis with multi-concurrent receiver GPR data

Dimitrios Angelis[1] | **Craig Warren[1]** | **Nectaria Diamanti[2]** | **James Martin[1]** |
A. Peter Annan[3]

[1]Department of Mechanical and Construction Engineering, Northumbria University, Newcastle upon Tyne, UK

[2]Department of Geophysics, Aristotle University of Thessaloniki, Thessaloniki, Greece

[3]Sensors & Software Inc., Mississauga, Canada

Correspondence
Dimitrios Angelis, Department of Mechanical and Construction Engineering, Northumbria University, Newcastle upon Tyne, NE1 8ST, UK.
Email: dimitrios.angelis@northumbria.ac.uk

Abstract

Determining subsurface electromagnetic (EM) wave velocity is critical for ground-penetrating radar (GPR) data analysis, as velocity is used for the time-to-depth conversion, and hence leads to obtaining the precise location of the objects of interest. Currently, the way to acquire detailed subsurface EM wave velocity models involves employing multi-offset GPR surveys, such as wide-angle reflection-refraction (WARR), in conjunction with normal moveout (NMO) based velocity analysis. Traditionally, these surveys are carried out using two separate transducers and were, therefore, time-consuming and had limited uptake. Recent advances in GPR hardware have allowed the development of novel systems with multi-concurrent sampling receivers, which enable rapid and dense acquisition of WARR data. These additional receivers increase the overall size, weight and cost of the system. Therefore, we investigated the effects of receiver arrangement on NMO-based velocity analysis and considered reducing the overall number of transducers, whilst maintaining satisfactory velocity spectra resolution and, hence, obtaining detailed stacking velocity models as well as improved stacked reflection sections. We used both simulated data from complex three-dimensional models as well as field data and examined different numbers and positions of receivers in different environments. Our results show that velocity spectra resolution can be maintained within acceptable limits whilst reducing the number of receivers from a configuration with seven equally spaced receivers, to a sparse configuration of four receivers. Thus, being able to decrease the number of receivers used by these new GPR systems will reduce both the total system weight and cost and, hopefully, increase their adoption for GPR surveys.

KEYWORDS
data processing, GPR, ground-penetrating radar, modelling, velocity

INTRODUCTION

Subsurface electromagnetic (EM) wave velocity models are critical to ground-penetrating radar (GPR) data analysis. Velocity is used to convert the two-way travel time of GPR pulses into depth as well as for other important processing steps including gain, static and dynamic corrections and migration (Annan, 2005; Forte & Pipan, 2017; Yilmaz, 2001). Moreover, the velocity information can be coupled with many suitable mixing models (Endres et al., 2009; Looyenga, 1965; Topp et al., 1980) to allow for the estimation of other subsurface properties, such as water content (Huisman et al., 2003; Klotzsche et al., 2018; Macheret et al., 1993; Murray et al., 2000) and porosity (Bradford, 2004; Bradford et al., 2009; Igel et al., 2013; Turesson, 2006). Currently, the most widely used method to determine detailed subsurface EM wave velocity models (including both vertical
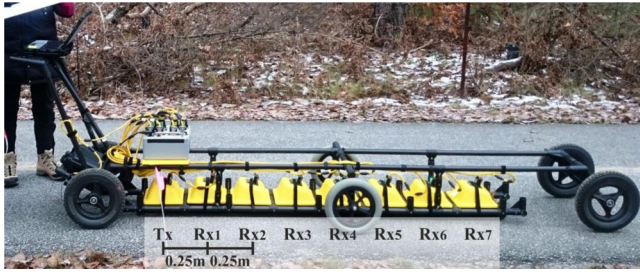
FIGURE 1 The 'WARR Machine' by Sensors & Software Inc., operating in a SmartCart transducer configuration.

and lateral variations) involves the employment of multi-fold (MF) GPR data acquisition modes, such as the wide-angle reflection-refraction (WARR) in conjunction with normal moveout (NMO) based velocity analysis using velocity spectra panels (Fisher et al., 1992; Greaves et al., 1996; Pipan et al., 1999; Nakashima et al., 2001; Becht et al., 2006; Murray et al., 2007; Booth et al., 2010; van der Kruk et al., 2010; De Domenico et al., 2013; Dal Bo et al., 2019; Church et al., 2020; Kaufmann et al., 2020; Angelis et al., 2022).

Despite their potential, WARR and the closely related common midpoint (CMP) GPR survey modes have seen limited adoption as few commercial GPR systems support separate transmitter (Tx) and receiver (Rx) transducers, and data collection is extremely time-consuming as they require multiple offsets which in turn translates into additional survey time and cost. Recent advances in GPR hardware have led to the development of multi-concurrent sampling receiver GPR systems, such as the 'WARR Machine' manufactured by Sensors & Software Inc. (Annan & Jackson, 2017; Diamanti et al., 2018) and shown in Figure 1. These systems allow for the rapid acquisition of multi-offset WARR soundings and can provide detailed velocity models as well as enhanced reflection sections (Kaufmann et al., 2020; Angelis et al., 2022). Nevertheless, such systems can require many transducers which significantly increases the total size and weight as well as power requirements, which in turn impacts the manoeuvrability and, therefore, the field conditions under these systems can be used. It also means an increase in cost compared to a simple single Tx–Rx system.

We have recently developed a detailed processing workflow (Figure 2) for data produced by multi-concurrent sampling receiver GPR systems and demonstrated that seven receivers are more than enough to provide detailed stacking velocity fields as well as enhanced zero-offset reflection sections (Angelis et al., 2022). In this study, we consider the effects of receiver arrangement (i.e., their number and positions) on the NMO-based velocity analysis. To achieve this, we have generated synthetic WARR GPR datasets which, along with field data from the 'WARR Machine', are used for our investigation. The paper begins with a short review of NMO-based velocity analysis, which also highlights the most important factors that can affect and, therefore, are relevant to receiver arrangement. We then investigate, using both synthetic and field data, the effect of receiver arrangement from a perspective of velocity spectra. Finally, in the last section of the paper, we validate our results by comparing the resultant stacking velocity fields as well as stacked sections of different transducer configurations.

NMO-BASED VELOCITY ANALYSIS

MF GPR WARR data can be rearranged through a coordinate transform into CMP gathers (i.e., small clusters of data that correspond to the same midpoint between different Tx–Rx pairs) (Figure 3). In a CMP gather, the reflection travel times $t(x)$ of a subsurface discontinuity follow a hyperbolic trajectory and are given by the NMO Equation 1:

$$t(x) = \sqrt{t_0^2 + \frac{x^2}{v^2}}, \qquad (1)$$

where t_0 is the zero-offset two-way travel time, x is the Tx–Rx offset and v is the NMO velocity.

Velocity analysis is based on the aforementioned equation and is performed using velocity spectra panels, usually in a selected number of CMP gathers, typically with a high signal-to-noise ratio (SNR). The one-dimensional velocity functions derived from this process are then interpolated into two-dimensional (2D) velocity cross sections (Yilmaz, 2001). The velocity spectrum is shown as a panel of velocity versus two-way travel time, in which the stacking results of the NMO-corrected CMP gather for different trial NMO velocities using Equation 1 are plotted side by side (Taner & Koehler, 1969). Velocity spectra indicate the optimum NMO velocity, also often referred to as stacking velocity, that is the velocity that will best flatten the hyperbolic event in the CMP gather and will allow optimal horizontal stacking (Mayne, 1962). Although stacking velocities do not directly correspond to the true material velocities, they can often be translated, under certain conditions (Yilmaz, 2001), into true material velocities using Dix (1955) formula (Fisher et al., 1992; Greaves et al., 1996; Murray et al., 2000, 2007; Huisman et al., 2003; Becht et al., 2006; Causse & Sénéchal, 2006; Booth, Clark, Hamilton, et al., 2010; Liu & Sato, 2012; Kaufmann et al., 2020).

There are several different coherency measures in calculating the velocity spectra which are well described by Yilmaz (2001). The most popular measure used in GPR is the normalized output-to-input energy ratio (NE), most often referred to as semblance (Neidell & Taner, 1971). Semblance as a process is straightforward, computationally efficient, and robust against noise (Zhou, 2014) and it is given by Equation 2:
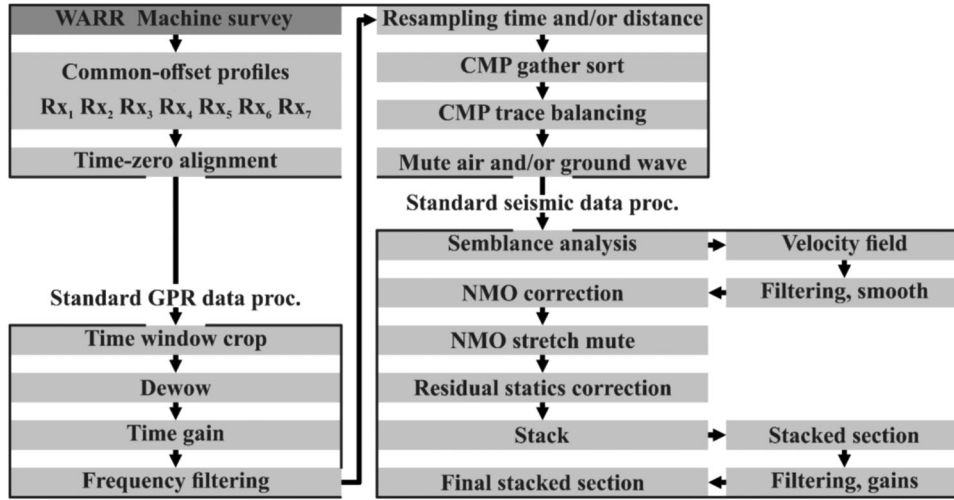
FIGURE 2 Processing workflow for multi-concurrent sampling receiver GPR data (Angelis et al., 2022).
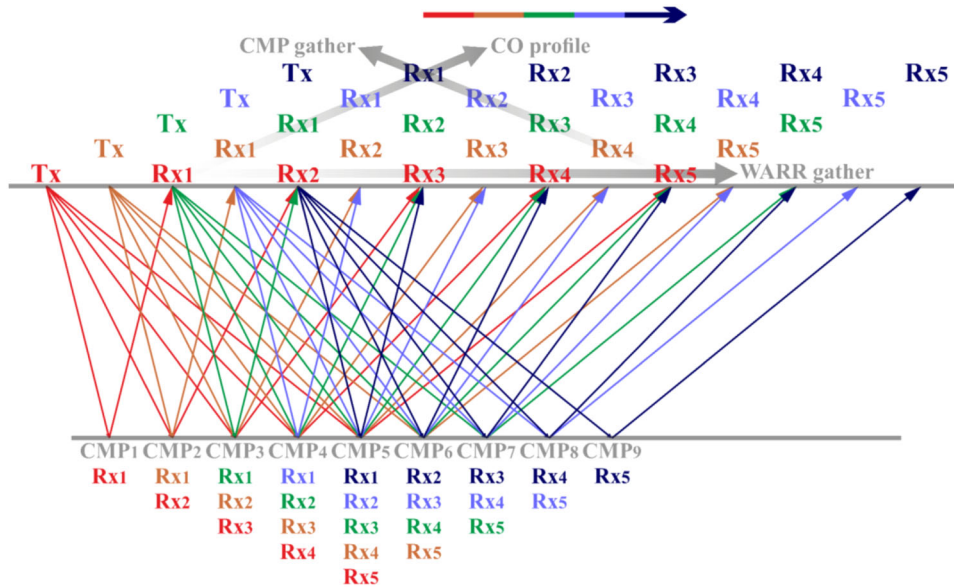
FIGURE 3 WARR data acquisition mode and CMP gather formulation.

$$S(c) = \frac{1}{F} \frac{\sum_{i=c-w/2}^{c+w/2} \left(\sum_{j=1}^{F} a(i,j)\right)^2}{\sum_{i=c-w/2}^{c+w/2} \sum_{j=1}^{F} a^2(i,j)}, \qquad (2)$$

where c is the centre of the time window w in which semblance is calculated, F denotes the number of traces (i.e., fold of the gather) and $a(i,j)$ is the amplitude of ith sample of the jth trace.

In general, velocity spectra resolution can be affected by several factors including the SNR of the CMP gather data, the spread length and the fold (Yilmaz, 2001). These factors clearly depend on the number and positioning of the transducers. Moreover, semblance as a measure of coherency is particularly sensitive to strong

amplitude versus offset (AVO) variations, and it does not handle them properly as it assumes constant amplitude models (Sarkar et al., 2001, 2002). This in turn can make the semblance analysis for GPR data problematic in case they are characterized by strong amplitude variations.

VELOCITY SPECTRA

Synthetic data

We used gprMax (Giannopoulos, 2005; Warren et al., 2016) to carry out the numerical simulations for this research. gprMax is an open-source EM wave

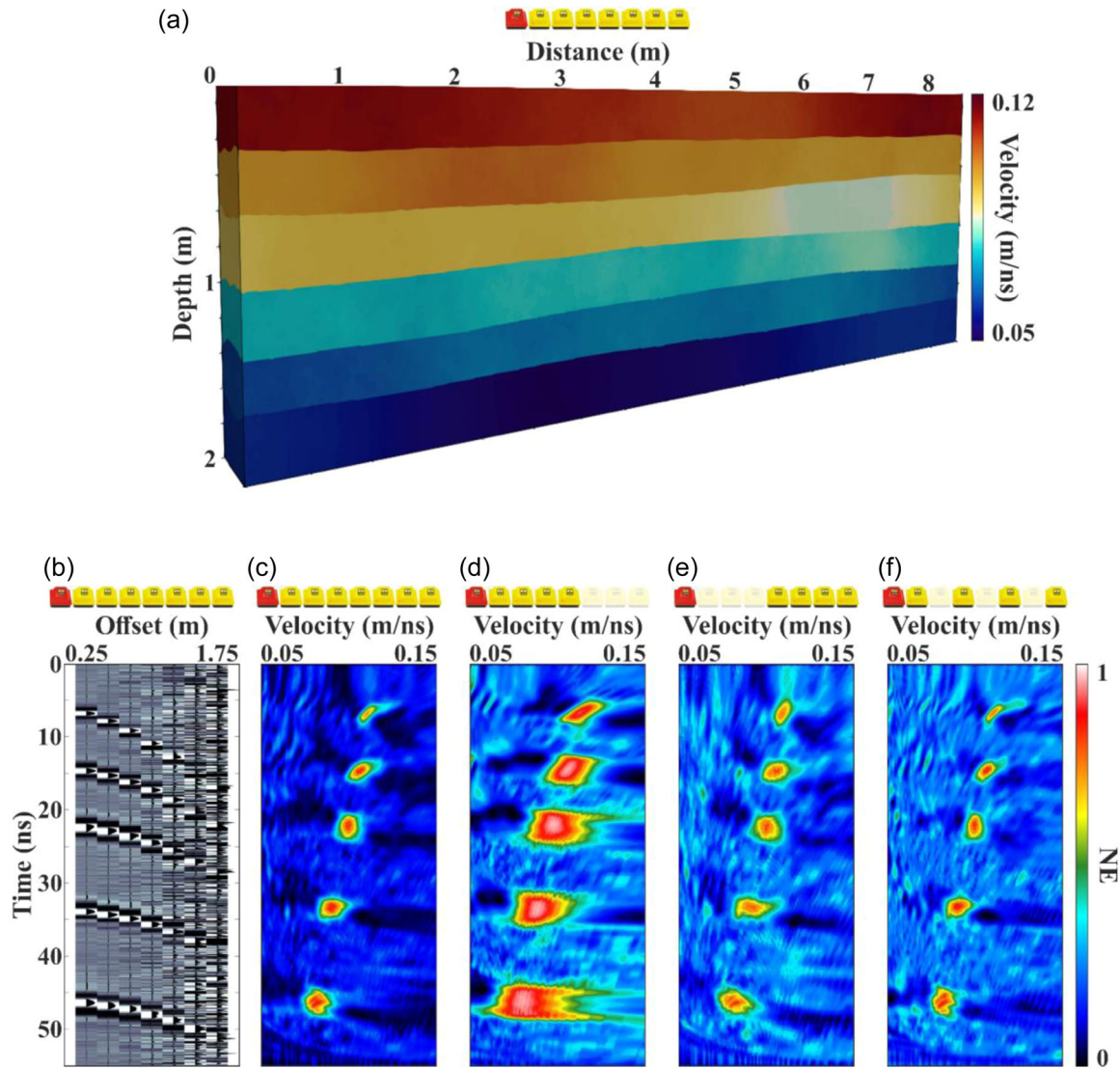**FIGURE 4** (a) Six-layered 3D model. Velocity decreases with depth and lateral velocity variations are also present. (b) 7Rx synthetic data CMP gather: Tx–Rx_1: 0.25 m, Rx separation: 0.25 m. (c) 7Rx semblance plot: Tx–Rx_1: 0.25 m, Rx separation: 0.25 m. (d) 4Rx semblance plot: Tx–Rx_1: 0.25 m, Rx separation: 0.25 m. (e) 4Rx semblance plot: Tx–Rx_1: 1.0 m, Rx separation: 0.25 m. (f) 4Rx semblance plot: Tx–Rx_1: 0.25 m, Rx separation: 0.5 m. At the top of each sub-figure the transducer configuration is shown, with the Tx depicted in red, and the Rxs in yellow.

simulator that solves Maxwell's equations, either in 2D or three-dimensional (3D) space, using the finite-difference time-domain method (Taflove & Hagness, 2005). The software incorporates many advanced modelling features and has become the de facto simulation tool for GPR, having been used successfully over many years by many researchers in academia and industry (Diamanti et al., 2017; Angelis et al., 2018; Jonard et al., 2019; Alani et al., 2020; Hamran et al., 2020; Luo et al., 2020; Giannakis et al., 2021).

Although we developed several 3D models with both simple and complex geometries considering different environments, we chose to use a layered cake model for this work, as we wanted to visualize the changes of the spectra peaks across multiple time intervals

(i.e., from shallow to deep events). Our model, shown in Figure 4a, is a six-layered 3D model with dimensions equal to 8 m × 0.7 m × 2 m (*x*, *y*, and *z* axes, respectively) in which the velocity decreases with depth. Each layer consists of heterogeneous soil with a stochastic distribution of the volumetric water fraction (Peplinski et al., 1995), providing additional lateral velocity variations. We used a single Hertzian dipole source with a waveform shaped as the first derivative of a Gaussian with a 500-MHz centre frequency, and we considered a transducer geometry similar to the 'WARR Machine' (i.e., one Tx and seven Rxs as shown in Figure 1). The distance between the source and the first receiver (Tx–Rx_1) as well as the distance between the subsequent receivers (Rx_n–Rx_{n+1}) was 0.25 m. The

trace step and time window were 0.025 m (Tx–Rx_1 / 10) and 55 ns, respectively. White Gaussian noise was added in post-processing to simulate the effects of a worst-case scenario of rapidly decreasing SNR with receiver offset. Although not all noise in real GPR data is random, the purpose of using such a scheme was to ensure that the synthetic data more closely represented the real data, in which noise can be problematic, especially at large offsets (Diamanti et al., 2018; Angelis et al., 2019). This has allowed visualizing the general changes in resolution of the semblance for different transducer configurations, particularly in scenarios with noisy or corrupted large offset traces.

A processed (with the basic steps of Figure 2) synthetic CMP gather consisting of seven traces from seven receivers (Tx–Rx_1 separation: 0.25 m, Rx_n–Rx_{n+1} separation: 0.25 m) is shown in Figure 4b, along with the computed semblance plot in Figure 4c. This is our baseline/reference model, which was designed to represent the Tx–Rx geometry of the real GPR system. There are five sharp peaks of medium to high strength in the semblance plot which correspond to the five different events seen in the CMP gather. We gradually removed traces from the CMP gather (i.e., to represent reducing the number of Rxs) and computed the corresponding semblance plots. We first removed the far-offset and then the near-offset traces (Figure 4d,e, respectively – transducer array on the top). Figure 4d shows the resultant semblance for the four near-offset traces with separation distances of Tx–Rx_1 = 0.25 m and Rx_n–Rx_{n+1} = 0.25 m. The first observation is that the semblance is generally noisier due to the decreased fold as only four traces are used for its computation. There is also a significant reduction in the sharpness of the peaks, which could, if they were more closely spaced, affect the ability to discriminate them but, more importantly, could lead to imprecise velocity estimations, especially if the picking process is performed manually. This reduction is caused by the lack of spread length (i.e., the transducer array covers a smaller area), and thus essentially the loss of moveout information. However, there is at the same time a significant increase in their strength, since only the high-SNR near-offset traces are involved in the computation. Figure 4e shows the semblance plot for the four far-offset traces with separation distances of Tx–Rx_1 = 1.0 m and Rx_n–Rx_{n+1} = 0.25 m. As in the previous case, the decreased fold introduces noise to the spectra. There is also some loss in sharpness of the peaks due to the far-offset traces having generally higher percentages of NMO stretch, as well as the loss of moveout information, though not as severe as in the previous case (Figure 4d) since moveout information is mostly obtained by the far-offset traces. Moreover, the strength of the peaks has been slightly reduced as the low-SNR far-offset traces are involved in the computation. These results illustrate the importance of both near-offset and far-offset traces in the computation of velocity spectra for GPR data, which is very similar to the one applied for seismic reflection data (Yilmaz, 2001). However, it should be mentioned that no severe degradation of the shallow peaks for the case of Figure 4e has been observed while this is usually present in seismic reflection data. A possible explanation is that with GPR, the NMO stretch percentage is lower due to the small transducer separation distances in GPR (i.e., this is in the order of a few centimetres to a metre while in seismic the geophone spacing is much larger).

Since our objective was to maintain the semblance resolution and sharpness of the velocity peaks as much as possible while reducing the number of receivers (i.e., the total number of traces in the CMP gather), and since the near- and far-offset traces play the most important role, we considered a sparse receiver configuration. Figure 4f illustrates the resultant semblance computed using again four traces with Tx–Rx_1 and Rx_n–Rx_{n+1} separation distance equal to 0.25 m and 0.5 m, respectively. When comparing the semblance panels in Figure 4c,f, both the sharpness and strength of the peaks are very similar while only a small and expected increase in the noise is observed in Figure 4f due to the fold reduction.

Field data

The same analysis was performed using field data collected with the 'WARR Machine', which, as previously mentioned, consists of one Tx and seven Rxs, all with 500 MHz centre frequency. The transducer separation was 0.25 m, and the trace step was 0.125 m (Tx–Rx_1/2). The data were collected at a test site used by Sensors & Software Inc., using the SmartCart configuration (Figure 1). The line crosses an asphalt-covered parking lot, a 1.3-m wide concrete sidewalk, a 5-m asphalt driveway, a concrete curb and ends after crossing a city street (Diamanti et al., 2018). This dataset was chosen for two reasons: firstly, because it is a standard test line where there is a vast amount of representative reference data; and, secondly, as it contains a mixture of complex and shallow reflections, therefore, making it particularly interesting for conducting velocity analysis.

The data were processed using a MATLAB-based software toolset (Angelis et al., 2020) using the aforementioned processing workflow (Figure 2). Figure 5a illustrates the processed common offset (CO) profile of the first receiver (Tx–Rx_1 separation: 0.25 m). Various annotations for the different subsurface features are also shown in this figure and highlighted with white arrows. Similarly, to the synthetic data example, Figure 5b,c shows a CMP gather (CMP 272) of the processed field data, which consists of seven traces from
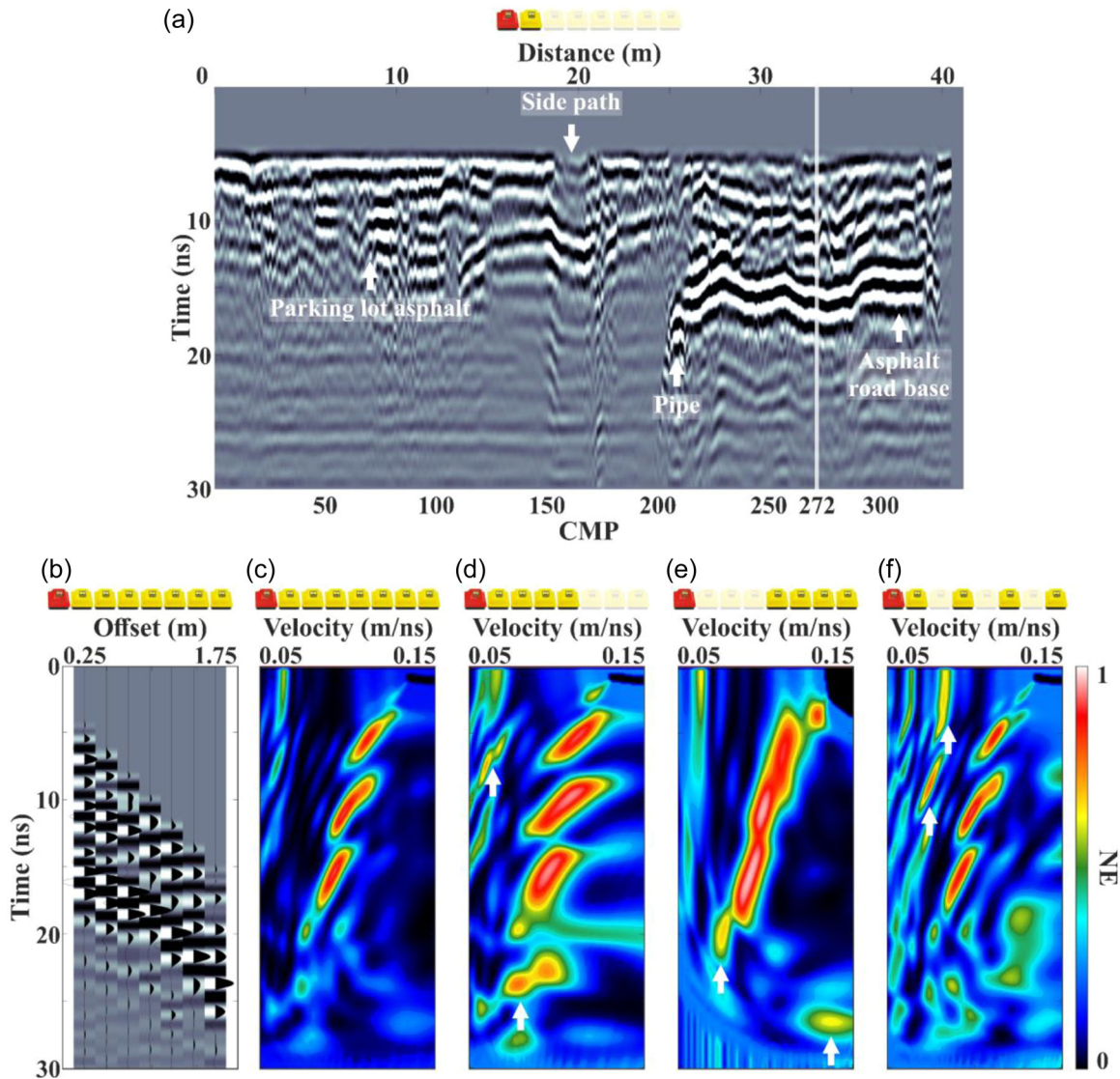
FIGURE 5 (a) Processed CO profile of the first receiver, Tx–Rx$_1$: 0.25 m. White arrows highlight the various subsurface features, and a white line the location of the investigated CMP gather. (b) 7Rx field data CMP gather (CMP 272): Tx–Rx$_1$: 0.25 m, Rx separation: 0.25 m. (c) 7Rx semblance plot: Tx–Rx$_1$: 0.25 m, Rx separation: 0.25 m. (d) 4Rx semblance plot: Tx–Rx$_1$: 0.25 m, Rx separation: 0.25 m. (e) 4Rx semblance plot: Tx–Rx$_1$: 1.0 m, Rx separation: 0.25 m. (f) 4Rx semblance plot: Tx–Rx$_1$: 0.25 m, Rx separation: 0.5 m. In (d)–(f) white arrows highlight some of the spurious semblance peaks. At the top of each sub-figure the transducer configuration is shown, with the Tx depicted in red, and the Rxs in yellow.

seven receivers (Tx–Rx$_1$ separation: 0.25 m, Rx$_n$–Rx$_{n+1}$ separation: 0.25 m), along with the respective semblance plot. This gather was chosen due to its complexity and particularly shallow reflections. There are three distinct and high-strength peaks in the semblance plot corresponding to the three reflected events in the CMP gather. Figure 5d–f shows the resultant semblance panels for traces with a near offset receiver configuration, a far offset receiver configuration, and a sparse receiver configuration, respectively. The first observation is that apart from the three distinct peaks seen in Figure 5c, and in contrast to the synthetic example, in all the semblance plots of Figure 5d–f for the different array configura-

tions, the noise and/or clutter due to the reduction of the fold becomes more consistent in the gather (as not all noise in real data is random) and, as a result, generates additional spurious medium to high strength semblance peaks (some of these extra peaks are marked with white arrows in Figure 5d–f). Although such peaks can be easily identified and skipped by a GPR interpreter through manual velocity picking, they could potentially be harmful during an automated picking process. The second and most important observation is the similarity in strength as well as in sharpness between the three main peaks produced by the four-receiver sparse configuration (Figure 5f) and by our baseline
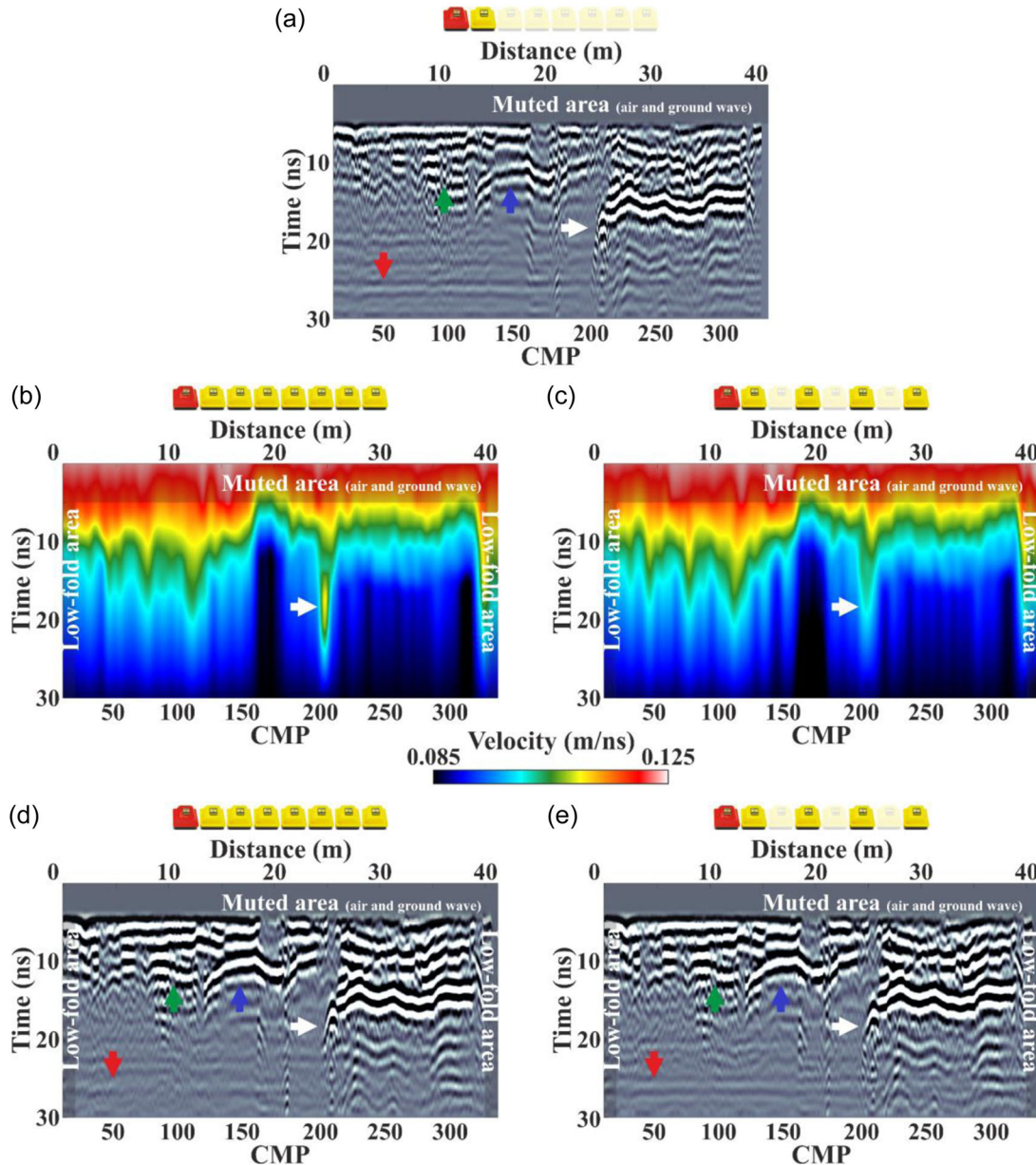
FIGURE 6 (a) Processed CO profile of the first receiver: $Tx–Rx_1$: 0.25 m. (b) Filtered stacking velocity field of the seven-receiver configuration. (c) Filtered stacking velocity field of the four-receiver sparse configuration. (d) NMO stacked zero-offset section of the seven-receiver configuration, derived using the respective velocity field of (b). (e) NMO stacked zero-offset section of the four-receiver configuration, derived using the respective velocity field of (c). In (b) and (c), white arrows highlight the area with different stacking velocities, and in (a), (d) and (e) the left-hand side of the pipe response. In (a), (d), and (e), the red arrow marks an area with attenuated horizontal ringing noise, the green arrow indicates a reflector with improved continuity, and the blue arrow shows an enhanced reflector. At the top of each sub-figure, the transducer configuration is shown, with the Tx depicted in red, and the Rxs in yellow.

seven-receiver configuration (Figure 5c). We observed the same behaviour in our synthetic data example as well.

VELOCITY FIELD AND STACKED SECTION

To investigate if it is feasible to extract a detailed, as well as accurate, stacking velocity field through the

sparse four-receiver configuration, we processed the data with our recently developed, automated velocity analysis picking algorithm (Angelis et al., 2022). To allow for a clear comparison between the two different transducer configurations and have a reference point, the data from the seven-receiver configuration were also processed in the same way. Although, as it was previously mentioned, velocity analysis is typically executed in selected high-SNR CMP gathers, we chose to perform
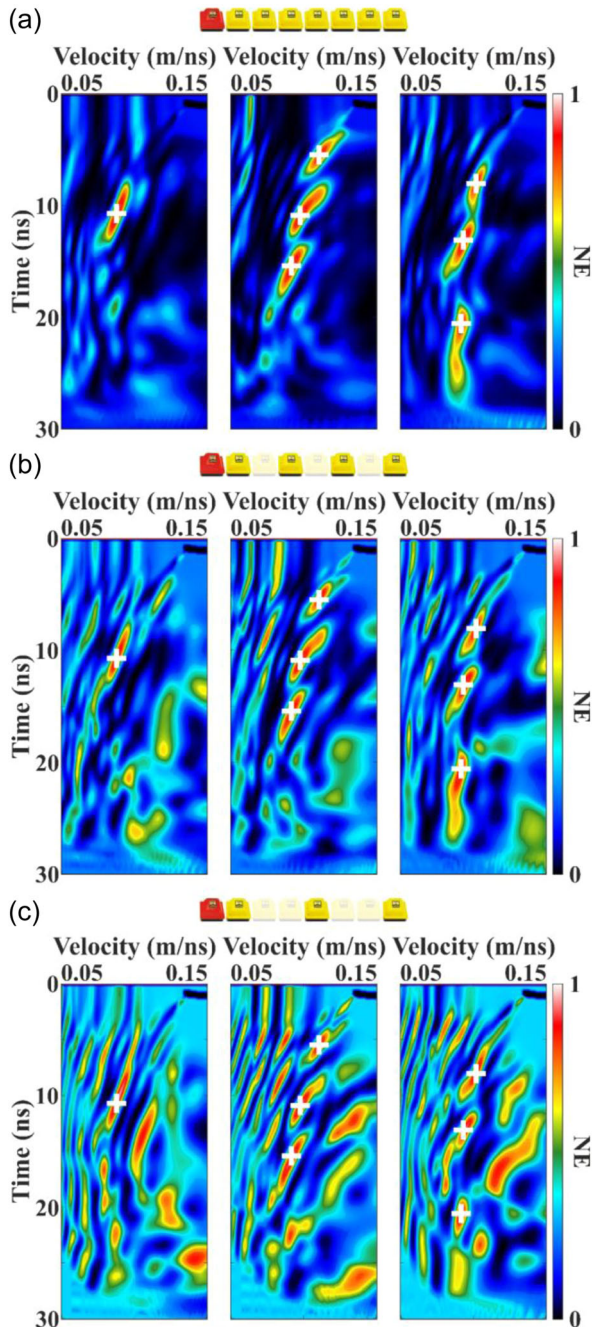
(a)

(b)

(c)

FIGURE 7 Corresponding semblance plot of CMP gather 154, 272 and 301. (a) 7Rx semblance plots: Tx–Rx$_1$: 0.25 m, Rx separation: 0.25 m. (b) 4Rx semblance plots: Tx–Rx$_1$: 0.25 m, Rx separation: 0.5 m. (c) 3Rx semblance plots: Tx–Rx$_1$: 0.25 m, Rx separation: 0.75 m. White crosses highlight the semblance peaks corresponding to the primary events. At the top of each sub-figure, the transducer configuration is shown, with the Tx depicted in red and the Rxs in yellow.

the analysis in all of the CMP gathers. This was done because the field data had multiple horizontal events across the whole survey line, as can be seen from the CO profile of the first receiver (Figure 6a), and, therefore, we wanted to compare results from both receiver configurations in as many different locations as possible.

Figure 6b,c depicts the resultant stacking velocity field for the seven-receiver configuration and the four-receiver sparse configuration, respectively. To create more realistic velocity fields (i.e., to remove velocity outliers), both alpha-trimmed mean filtering and 2D Gaussian smoothing were applied to the data. From Figure 6b,c, it can be observed that there is a strong correlation between the two velocity fields along the whole survey line, with almost all high- as well as low-velocity areas coinciding. There are a few exceptions such as the small area at approximately 25 m along the x-axis which is marked with white arrows. The medium stacking velocities which are observed in this area, and only in Figure 6b, are due to the left-hand side of the hyperbola produced by a pipe located in the subsurface. Although these velocities are absent in the resultant field of the four-receiver sparse configuration, at this point we would like to remind the reader that both velocity fields are produced using an automated velocity picking algorithm. Errors such as this one could potentially be corrected afterwards through a manual repicking process, which is common practice anyway.

To validate our results, each field was used to stack the corresponding data of the two different transducer configurations. Figure 6d,e depicts the resultant NMO corrected, zero-offset, stacked sections for the seven-receiver configuration and the four-receiver sparse configuration, respectively, while to allow a comparison, the CO profile of the first receiver is also shown in Figure 6a. As expected, by comparing the stacked section of the seven-receiver configuration (Figure 6d) with the CO profile of the first receiver (Figure 6a), one can see that there is a significant reduction of clutter, including a slight attenuation of horizontal ringing noise (e.g., the area marked with a red arrow), improved reflector continuity (e.g., reflector indicated with a green arrow), as well as a significant enhancement of reflectors that previously were not fully visible (e.g., reflector highlighted with a blue arrow), all these being the benefits expected from the stacking procedure. Interestingly, by comparing the respective stacked section of the reduced four-receiver configuration (Figure 6e) with the CO profile of the first receiver (Figure 6a) similar results are observed. It has to be noted that the improvement is not as good as in the case of the seven-receiver configuration, which is expected due to the reduction of the fold. The above results validate both stacking velocity fields and, consequently, illustrate that even the four-receiver sparse configuration can not only allow for detailed stacking velocity fields but also lead to enhanced zero-offset reflection sections.

DISCUSSION

Our main aim was to investigate the feasibility of reducing the number of transducers of newly developed
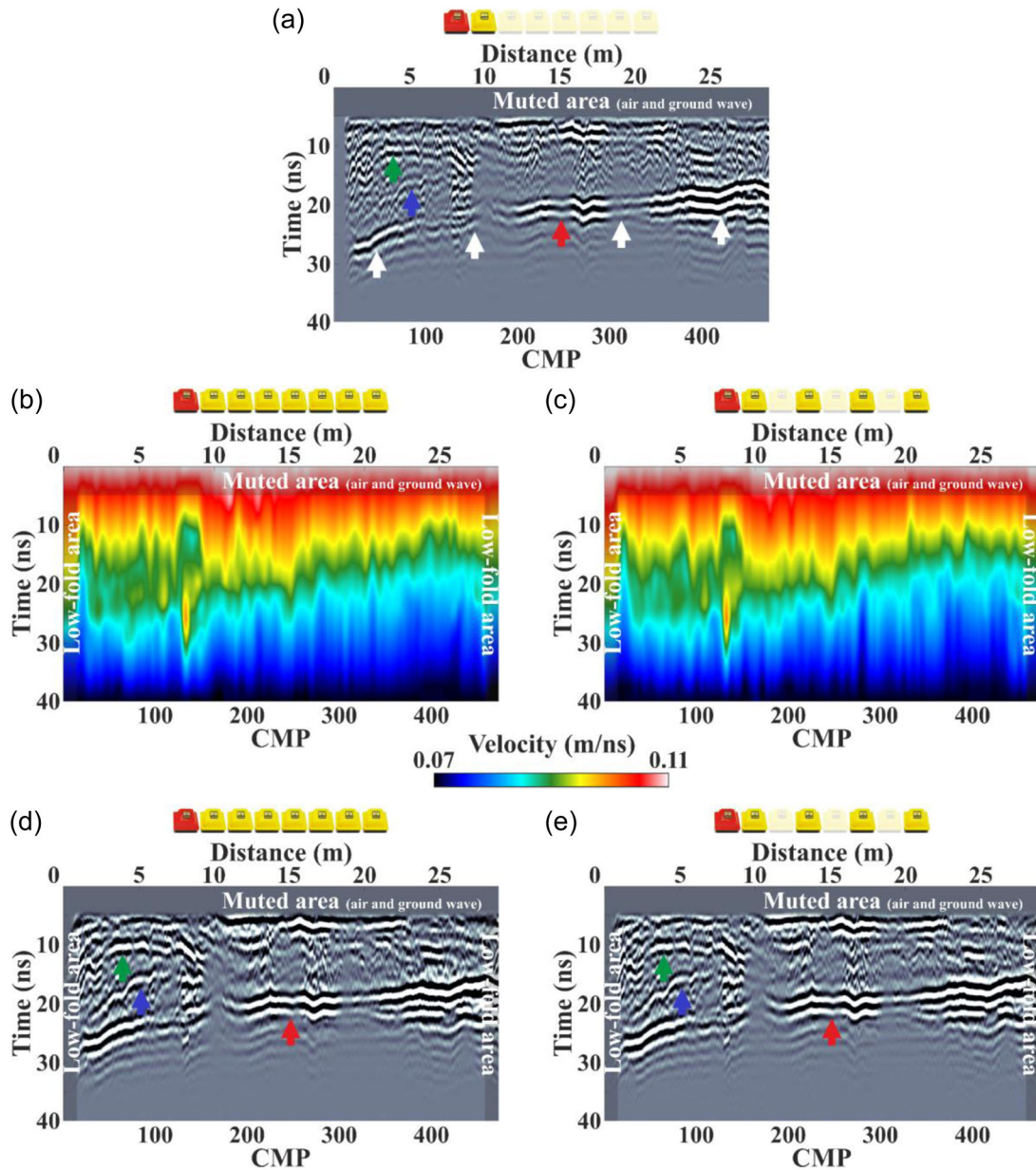
FIGURE 8 (a) Processed CO profile of the first receiver: $Tx–Rx_1$: 0.25 m. (b) Filtered stacking velocity field of the seven-receiver configuration. (c) Filtered stacking velocity field of the four-receiver sparse configuration. (d) NMO stacked zero-offset section of the seven-receiver configuration, derived using the respective velocity field of (b). (e) NMO stacked zero-offset section of the four-receiver configuration, derived using the respective velocity field of (c). In (a), white arrows highlight the linear pipe response. In (a), (d) and (e), the red arrow marks an area with reduced ringing noise (reverberation of the GPR wave in the pipe), the green arrow indicates a reflector with improved continuity and the blue arrow shows an enhanced reflector. At the top of each sub-figure, the transducer configuration is shown, with the Tx depicted in red and the Rxs in yellow.

multi-concurrent receiver GPR systems while maintaining satisfactory velocity spectra resolution and, consequently, deriving detailed stacking velocity fields through not only a manual but most importantly, an automated velocity picking process. We have demonstrated that this is possible using a four-receiver sparse configuration.

Nevertheless, it should be stressed that key processing steps such as the time-zero alignment and CMP trace balancing (Angelis et al., 2022; Kaufmann et al., 2020) must be carefully performed. Minor misalignments of a few samples (of the order of tenths of nanoseconds) in some of the CMP gather traces, which could be caused by inaccurate first break picking, do not have a significant effect on the semblance analysis of a gather consisting of seven traces (i.e., seven-receiver configuration); however, they become detrimental as the number of traces decreases (e.g., four-receiver configuration). As a result, additional manual first break

corrections could be required. Furthermore, as the number of traces decreases in the CMP gather, the main hyperbolic events can be stair-cased and potentially mix with responses from other events which are always present. As a result, they will make a sliding window type of trace-balancing technique much more difficult to implement, and, therefore, much more experimentation for this step with different time gates could be required. In addition, due to the reduction of the fold, even if the aforementioned key processing steps are performed correctly, there will still be spurious peaks across multiple velocity spectra, as shown in our examples (white arrows in Figure 5f). Such peaks, which are usually of medium strength, can be avoided by increasing the threshold of the automated picking algorithm (Angelis et al., 2022) or even by muting parts of the velocity spectrum panel. However, by doing so, other potentially useful peaks of medium strength could be skipped/sacrificed, and, consequently, velocity analysis will be based only on the high-strength peaks (see the case of the pipe presented above, in Figure 6b,c – white arrows). Hence, re-adjusting the parameters of the automatic velocity picking algorithm several times in the same data set and/or even conducting additional manual velocity re-picking could also be required.

We also performed the same experiments using a three-receiver sparse configuration; however, it quickly became evident that automated velocity analysis of three-fold CMP gathers was practically impossible, as the corresponding semblance plots were governed by multiple spurious peaks. This can be seen in Figure 7, which shows the resultant semblance plots of three different CMP gathers (CMP 154, 272 and 301) for the aforementioned transducer configurations.

The analysis presented so far has been applied to multiple datasets collected in various environments. In Figure 8, we include one of those additional datasets with the results, that is, the corresponding stacking velocity fields and NMO stacked zero-offset sections for the seven-receiver configuration as well as for the four-receiver sparse configuration. The data shown in Figure 8 were acquired over an asphalt-covered parking lot, and the target of interest was a linear pipe (white arrows in Figure 8a). Additional information about this dataset (i.e., acquisition parameters, area description and targets) can be found in Angelis et al. (2022). The results from this additional dataset also confirm that a system with a four-receiver sparse configuration is shown to have the minimum acceptable number of Rxs that is needed to obtain acceptable velocity fields as well as enhanced stacked reflection sections.

It is possible that our results can be further improved by exploiting the high volume of data that can be generated by these new, multi-concurrent GPR systems, like, for example, by increasing the number of CMP gathers per unit distance. We took advantage of this fact and used the increased amount of data to filter the velocity

outliers of the resultant stacking velocity fields. Additionally, techniques such as spatial semblance averaging could be used to suppress the spurious peaks (Diamanti et al., 2018).

CONCLUSION

Newly developed multi-concurrent GPR systems, such as the 'WARR Machine', have the ability to acquire extremely fast, dense, multi-offset data and thus provide benefits such as detailed stacking velocity fields and enhanced zero-offset reflection sections. However, they can require many transducers, a fact that leads to increasing the size, weight, power requirements, and cost of the GPR system. We used both simulated data from complex 3D models as well as field data from the GPR 'WARR Machine' to investigate the quality of velocity spectra responses with different receiver arrangements. Using a system that is comprised of 1 Tx and 7 Rxs as a baseline, we calculated semblance plots for both numerical and field data. We then reduced the number of receivers by removing traces from the CMP gather, and these results showed that we could obtain similar velocity spectra to the seven Rx baseline, including maintaining the sharpness of the semblance peaks. To further validate the results from this sparse four-receiver configuration, we processed data both from this suggested configuration and the seven-receiver configuration with an automated velocity analysis tool that was developed for the purpose of this work. Through this process, we obtained similar velocity fields as well as enhanced stacked reflection sections for both cases. By reducing the number of receivers and hence, the weight of these novel GPR systems, they will become more practicable and cost-effective. This should lead to more widespread adoption and improved subsurface velocity models that will become standard practice.

REFERENCES
Alani, A.M., Giannakis, I., Zou, L., Lantini, L. & Tosti, F. (2020) Reverse-time migration for evaluating the internal structure of tree-trunks using ground-penetrating radar. *NDT & E International*, 115, 102294. https://doi.org/10.1016/j.ndteint.2020.102294
Angelis, D., Tsourlos, P., Tsokas, G., Vargemezis, G., Zacharopoulou, G. & Power, C. (2018) Combined application of GPR and ERT for the assessment of a wall structure at the Heptapyrgion fortress

(Thessaloniki, Greece). *Journal of Applied Geophysics*, 152, 208–220. https://doi.org/10.1016/j.jappgeo.2018.04.003

Angelis, D., Warren, C. & Diamanti, N. (2020) A software toolset for processing and visualization of single and multi-offset GPR data. In: *18th International Conference on Ground Penetrating Radar*, Golden, CO, 14–19 June 2020. Houston, TX: Society of Exploration Geophysicists, pp. 320–323. https://doi.org/10.1190/gpr2020-084.1

Angelis, D., Warren, C. & Diamanti, N. (2019) Preliminary development of a workflow for processing multi-concurrent receiver GPR data. In: *10th International Workshop on Advanced Ground Penetrating Radar*. Bunnik, The Netherlands: European Association of Geoscientists & Engineers, vol. 1, pp. 1–7. https://doi.org/10.3997/2214-4609.201902572

Angelis, D., Warren, C., Diamanti, N., Martin, J. & Annan, A.P. (2022) Development of a workflow for processing gpr data from multi-concurrent receivers. *Geophysics*, 87(4), WB9–WB18. https://doi.org/10.1190/geo2021-0376.1

Annan, A.P. (2005) 11. Ground-penetrating radar. In: *Near-surface geophysics* (pp. 357–438.). Society of Exploration Geophysicists. https://doi.org/10.1190/1.9781560801719.ch11

Annan, A.P. & Jackson, S.R. (2017) The WARR Machine. In: *2017 9th International Workshop on Advanced Ground Penetrating Radar, IWAGPR 2017 - Proceedings*. Piscataway, NJ: IEEE, pp. 1–4. https://doi.org/10.1109/IWAGPR.2017.7996106

Becht, A., Appel, E. & Dietrich, P. (2006) Analysis of multi-offset GPR data: A case study in a coarse-grained gravel aquifer. *Near Surface Geophysics*, 4(4), 227–240. https://doi.org/10.3997/1873-0604.2005047

Booth, A.D., Clark, R.A., Hamilton, K. & Murray, T. (2010) Multi-offset ground penetrating radar methods to image buried foundations of a Medieval Town Wall, Great Yarmouth, UK. *Archaeological Prospection*, 17(2), 103–116. https://doi.org/10.1002/arp.377

Booth, A.D., Clark, R.A. & Murray, T. (2010) Semblance response to a ground-penetrating radar wavelet and resulting errors in velocity analysis. *Near Surface Geophysics*, 8(3), 235–246. https://doi.org/10.3997/1873-0604.2010008

Bradford, J.H. (2004) 3D multi-offset, multi-polarization acquisition and processing of GPR data: A controlled DNAPL spill experiment. In: *Symposium on the Application of Geophysics to Engineering and Environmental Problems 2004*. Denver, CO: Environment and Engineering Geophysical Society, pp. 514–527. https://doi.org/10.4133/1.2923365

Bradford, J.H., Clement, W.P. & Barrash, W. (2009) Estimating porosity with ground-penetrating radar reflection tomography: A controlled 3-D experiment at the Boise Hydrogeophysical Research Site. *Water Resources Research*, 45(4), https://doi.org/10.1029/2008WR006960

Causse, E. & Sénéchal, P. (2006) Model-based automatic dense velocity analysis of GPR field data for the estimation of soil properties. *Journal of Geophysics and Engineering*, 3(2), 169–176. https://doi.org/10.1088/1742-2132/3/2/008

Church, G., Grab, M., Schmelzbach, C., Bauder, A. & Maurer, H. (2020) Monitoring the seasonal changes of an englacial conduit network using repeated ground-penetrating radar measurements. *Cryosphere*, 14(10), 3269–3286. https://doi.org/10.5194/tc-14-3269-2020

Dal Bo, I., Klotzsche, A., Schaller, M., Ehlers, T.A., Kaufmann, M.S., Fuentes Espoz, J.P. et al. (2019) Geophysical imaging of regolith in landscapes along a climate and vegetation gradient in the Chilean coastal cordillera. *Catena*, 180, 146–159. https://doi.org/10.1016/j.catena.2019.04.023

De Domenico, D., Teramo, A. & Campo, D. (2013) GPR surveys for the characterization of foundation plinths within a seismic vulnerability analysis. *Journal of Geophysics and Engineering*, 10(3),. https://doi.org/10.1088/1742-2132/10/3/034007

Diamanti, N., Annan, A.P. & Redman, J.D. (2017) Concrete bridge deck deterioration assessment using ground penetrating radar (GPR). *Journal of Environmental and Engineering Geophysics*, 22(2), 121–132. https://doi.org/10.2113/JEEG22.2.121

Diamanti, N., Judith Elliott, E., Jackson, S.R. & Peter Annan, A. (2018) The WARR Machine: System design, implementation and data. *Journal of Environmental and Engineering Geophysics*, 23(4), 469–487. https://doi.org/10.2113/JEEG23.4.469

Dix, C.H. (1955) Seismic velocities from surface measurements. *Geophysics*, 20(1), 68–86. https://doi.org/10.1190/1.1438126

Endres, A.L., Murray, T., Booth, A.D. & West, L.J. (2009) A new framework for estimating englacial water content and pore geometry using combined radar and seismic wave velocities. *Geophysical Research Letters*, 36(4), https://doi.org/10.1029/2008GL036876

Fisher, E., McMechan, G.A. & Annan, A.P. (1992) Acquisition and processing of wide-aperture ground-penetrating radar data. *Geophysics*, 57(3), 495–504. https://doi.org/10.1190/1.1443265

Forte, E. & Pipan, M. (2017) Review of multi-offset GPR applications: Data acquisition, processing and analysis. *Signal Processing*, 132, 210–220. https://doi.org/10.1016/j.sigpro.2016.04.011

Giannakis, I., Giannopoulos, A. & Warren, C. (2021) A machine learning scheme for estimating the diameter of reinforcing bars using ground penetrating radar. *IEEE Geoscience and Remote Sensing Letters*, 18(3), 461–465. https://doi.org/10.1109/LGRS.2020.2977505

Giannopoulos, A. (2005) Modelling ground penetrating radar by GprMax. *Construction and Building Materials*, 19(10), 755–762. https://doi.org/10.1016/j.conbuildmat.2005.06.007

Greaves, R.J., Lesmes, D.P., Lee, J.M. & Toksöz, M.N. (1996) Velocity variations and water content estimated from multi-offset, ground-penetrating radar. *Geophysics*, 61(3), 683–695. https://doi.org/10.1190/1.1443996

Hamran, S.E., Paige, D.A., Amundsen, H.E.F., Berger, T., Brovoll, S., Carter, L. et al. (2020) Radar imager for Mars' subsurface experiment—RIMFAX. *Space Science Reviews*, 216(8), 128. https://doi.org/10.1007/s11214-020-00740-4

Huisman, J.A., Hubbard, S.S., Redman, J.D. & Annan, A.P. (2003) Measuring soil water content with ground penetrating radar: a review. *Vadose Zone Journal*, 2(4), 476–491. https://doi.org/10.2113/2.4.476

Igel, J., Günther, T. & Kuntzer, M. (2013) Ground-penetrating radar insight into a coastal aquifer: The freshwater lens of Borkum Island. *Hydrology and Earth System Sciences*, 17(2), 519–531. https://doi.org/10.5194/hess-17-519-2013

Jonard, F., Andre, F., Pinel, N., Warren, C., Vereecken, H. & Lambot, S. (2019) Modeling of multilayered media Green's functions with rough interfaces. *IEEE Transactions on Geoscience and Remote Sensing*, 57(10), 7671–7681. https://doi.org/10.1109/TGRS.2019.2915676

Kaufmann, M.S., Klotzsche, A., Vereecken, H. & van der Kruk, J. (2020) Simultaneous multichannel multi-offset ground-penetrating radar measurements for soil characterization. *Vadose Zone Journal*, 19(1), e20017. https://doi.org/10.1002/vzj2.20017

Klotzsche, A., Jonard, F., Looms, M.C., van der Kruk, J. & Huisman, J.A. (2018) Measuring soil water content with ground penetrating radar: a decade of progress. *Vadose Zone Journal*, 17(1), 180052. https://doi.org/10.2136/vzj2018.03.0052

Liu, H. & Sato, M. (2012) Dynamic groundwater level estimation by the velocity spectrum analysis of GPR. In: *2012 14th International Conference on Ground Penetrating Radar, GPR 2012*. Piscataway, NJ: IEEE, pp. 413–418. https://doi.org/10.1109/icgpr.2012.6254901

Looyenga, H. (1965) Dielectric constants of heterogeneous mixtures. *Physica*, 31(3), 401–406. https://doi.org/10.1016/0031-8914(65)90045-5

Luo, T.X.H., Lai, W.W.L. & Giannopoulos, A. (2020) Forward modelling on GPR responses of subsurface air voids. *Tunnelling and Underground Space Technology*, 103, 103521. https://doi.org/10.1016/j.tust.2020.103521

Macheret, Y.Y., Moskalevsky, M.Y. & Vasilenko, E.V. (1993) Velocity of radio waves in glaciers as an indicator of their hydrothermal state, structure and regime. *Journal of Glaciology*, 39(132), 373–384. https://doi.org/10.3189/s0022143000016038

Mayne, W.H. (1962) Common reflection point horizontal data stacking techniques. *Geophysics*, 27(6), 927–938. https://doi.org/10.1190/1.1439118

Murray, T., Booth, A.D. & Rippin, D.M. (2007) Water-content of glacier-ice: limitations on estimates from velocity analysis of surface ground-penetrating radar surveys. *Journal of Environmental and Engineering Geophysics*, 12(1), 87–99. https://doi.org/10.2113/JEEG12.1.87

Murray, T., Stuart, G.W., Fry, M., Gamble, N.H. & Crabtree, M.D. (2000) Englacial water distribution in a temperate glacier from surface and borehole radar velocity analysis. *Journal of Glaciology*, 46(154), 389–398. https://doi.org/10.3189/172756500781833188

Nakashima, Y., Zhou, H. & Sato, M. (2001) Estimation of groundwater level by GPR in an area with multiple ambiguous reflections. *Journal of Applied Geophysics*, 47(3–4), 241–249. https://doi.org/10.1016/S0926-9851(01)00068-4

Neidell, N.S. & Taner, M.T. (1971) Semblance and other coherency measures for multichannel data. *Geophysics*, 36(3), 482–497. https://doi.org/10.1190/1.1440186

Peplinski, N.R., Ulaby, F.T. & Dobson, M.C. (1995) Dielectric properties of soils in the 0.3–1.3-GHz range. *IEEE Transactions on Geoscience and Remote Sensing*, 33(3), 803–807. https://doi.org/10.1109/36.387598

Pipan, M., Baradello, L., Forte, E., Prizzon, A. & Finetti, I. (1999) 2-D and 3-D processing and interpretation of multi-fold ground penetrating radar data: a case history from an archaeological site. *Journal of Applied Geophysics*, 41(2–3), 271–292. https://doi.org/10.1016/S0926-9851(98)00047-0

Sarkar, D., Baumel, R.T. & Larner, K.L. (2002) Velocity analysis in the presence of amplitude variation. *Geophysics*, 67(5), 1664–1672. https://doi.org/10.1190/1.1512814

Sarkar, D., Castagna, J.P. & Lamb, W.J. (2001) AVO and velocity analysis. *Geophysics*, 66(4), 1284–1293. https://doi.org/10.1190/1.1487076

Taflove, A. & Hagness, S.C. (2005) In: *Computational electrodynamics: The finite-difference time-domain method* (3rd ed.). Boston, MA: Artech House. https://us.artechhouse.com/Computational-Electrodynamics-Third-Edition-P1929.aspx

Taner, M.T. & Koehler, F. (1969) Velocity spectra. Digital computer derivation and applications of velocity functions. *Geophysics*, 34(6), 859–881. https://doi.org/10.1190/1.1440058

Topp, G.C., Davis, J.L. & Annan, A.P. (1980) Electromagnetic determination of soil water content: Measurements in coaxial transmission lines. *Water Resources Research*, 16(3), 574–582. https://doi.org/10.1029/WR016i003p00574

Turesson, A. (2006) Water content and porosity estimated from ground-penetrating radar and resistivity. *Journal of Applied Geophysics*, 58(2), 99–111. https://doi.org/10.1016/j.jappgeo.2005.04.004

van der Kruk, J., Jacob, R.W. & Vereecken, H. (2010) Properties of precipitation-induced multilayer surface waveguides derived from inversion of dispersive TE and TM GPR data. *Geophysics*, 75(4), WA263–WA273. https://doi.org/10.1190/1.3467444

Warren, C., Giannopoulos, A. & Giannakis, I. (2016) gprMax: Open source software to simulate electromagnetic wave propagation for Ground Penetrating Radar. *Computer Physics Communications*, 209, 163–170. https://doi.org/10.1016/j.cpc.2016.08.020

Yilmaz, Ö. (2001) Seismic data analysis. In: *Seismic data analysis*. Houston, TX: Society of Exploration Geophysicists. https://doi.org/10.1190/1.9781560801580

Zhou, H.-W. (2014) Practical seismic data analysis. In: *Practical seismic data analysis*. Cambridge, UK: Cambridge University Press. https://doi.org/10.1017/cbo9781139027090